

# The impact of semimetal nanoparticles on the conduction of thick glass layer at Ag/Si contact interface <sup>EP</sup>

Cite as: J. Appl. Phys. **127**, 225302 (2020); <https://doi.org/10.1063/5.0001488>

Submitted: 20 January 2020 . Accepted: 26 May 2020 . Published Online: 08 June 2020

Keming Ren <sup>id</sup>, Dan Han <sup>id</sup>, Tang Ye <sup>id</sup>, Yong Zhang <sup>id</sup>, and Abasifreke Ebong <sup>id</sup>

## COLLECTIONS

<sup>EP</sup> This paper was selected as an Editor's Pick



View Online



Export Citation



CrossMark

Lock-in Amplifiers  
up to 600 MHz



# The impact of semimetal nanoparticles on the conduction of thick glass layer at Ag/Si contact interface



Cite as: J. Appl. Phys. 127, 225302 (2020); doi: 10.1063/5.0001488

Submitted: 20 January 2020 · Accepted: 26 May 2020 ·

Published Online: 8 June 2020



Keming Ren,<sup>1,a)</sup> Dan Han,<sup>2</sup> Tang Ye,<sup>1</sup> Yong Zhang,<sup>3</sup> and Abasifreke Ebong<sup>3</sup>

## AFFILIATIONS

<sup>1</sup>Department of Chemistry, University of North Carolina at Charlotte, Charlotte, North Carolina 28223, USA

<sup>2</sup>Department of Mathematics, University of Louisville, Louisville, Kentucky 40292, USA

<sup>3</sup>Department of Electrical and Computer Engineering, University of North Carolina at Charlotte, Charlotte, North Carolina 28223, USA

<sup>a)</sup>Author to whom correspondence should be addressed: kren@uncc.edu

## ABSTRACT

This paper reports on the ohmic contact formed by the conductive glass layer found at the interface of Ag/Si contacts on lowly doped emitter silicon solar cells due to the presence of semimetal nanoparticles. The scanning electron microscopy and scanning transmission electron microscope analyses revealed an interface glass layer (IGL) thickness of greater than 380 nm, which was enriched with micro-sized alloys composed of semimetal nanoparticles. This IGL was conductive as confirmed by conductive atomic force microscopy (C-AFM). The presence of these semimetal nanoparticles, identified as Ag<sub>2</sub>Te and PbTe, was both endowed with low bandgap energies as confirmed by Raman spectroscopy and energy dispersive x-ray spectroscopy. These semimetal nanoparticles were found only in the IGL and formed a “bridge” to connect the Ag gridline and Si emitter for carrier transport. Based on the modified Fowler–Nordheim tunneling process, the modeled C-AFM I–V characteristic curve showed a barrier height of 0.1 eV corresponding to an IGL thickness of only 18 nm. Thus, the carrier transport mechanism “through the conductive bridge” was formed by the semimetal nanoparticles embedded in the IGL. Therefore, the high conductivity of the interface glass led to the specific contact resistance to be independent of the emitter peak doping concentration.

Published under license by AIP Publishing. <https://doi.org/10.1063/5.0001488>

## I. INTRODUCTION

The high-throughput and low-cost attributes of the screen-printing technology have constrained the front gridlines of the commercial Si solar cells to be formed with the Ag paste. The Ag paste is applied through the use of screens with narrow openings constituting the gridlines and busbars onto the Si wafers, which have previously been coated with SiN<sub>x</sub> antireflective coating (ARC) and later followed by rapid thermal processing under a high peak temperature for a short time. During rapid thermal processes, (i) the glass frits in the Ag paste melt and etch the ARC through redox reactions, (ii) then the molten glass dissolves the Ag metal by forming silver-lead alloys<sup>1</sup> and further reacts with Si to dissolve [100] Si planes, and (iii) after cooling, an interface glass layer (IGL) is formed between the Ag gridline and the Si emitter with Ag particles<sup>2,3</sup> embedded in the IGL. Ag crystallites<sup>4</sup> are found on the [111] planes of the inverted pyramids<sup>1</sup> precipitated in the Si emitter

underneath the IGL. The thickness of the IGL depends on the (a) solid Ag particle size,<sup>5</sup> (b) the composition of the glass frits,<sup>6,7</sup> (c) the additives<sup>8,9</sup> in the paste to control the sintering of the Ag particles, and (d) the firing conditions.<sup>10–12</sup>

The IGL thickness has a direct impact on the carrier transport path at the Ag/Si interface. Based on the microstructure of the Ag/Si contact, two carrier transport paths from the Si emitter to the Ag gridline are identified: (1) direct contact with Ag crystallites (“through Ag crystallites”)<sup>10,13–15</sup> and (2) tunneling through an ultrathin IGL<sup>16</sup> or nanoparticle assisted tunneling (“through ultrathin IGL”).<sup>3,17</sup> In addition, it was found that forming gas anneal after sintering enhanced metallic precipitates in the IGL, and hence, these precipitates increase the conductivity of glass through multistep tunneling.<sup>18</sup> Thus, either thin IGL or IGL embedded with high metal precipitates is preferred for the ease of carrier transport at the Ag/Si interface.

As predicted by the International Technology Roadmap for Photovoltaic (ITRPV),<sup>19</sup> the lowly doped emitter (140  $\Omega/\text{sq}$ ) is the sure pathway to increase the efficiency of a solar cell due to the decrease in the surface recombination and higher transparency to photons. Thus, understanding of how to form a low contact resistance with appropriate current transport paths is required for the lowly doped emitter. The two carrier transport paths have been well studied by experimental measurements<sup>10,14</sup> and theoretical calculations.<sup>15,20,21</sup> Under the “through Ag crystallites,” the specific contact resistance ( $\rho_c$ ) of the Ag crystallite contact depends strongly on the emitter surface doping concentration (ND). Low  $\rho_c$  was demonstrated through field emission on a heavily doped emitter<sup>22</sup> of ND  $\geq 1 \times 10^{20} \text{ cm}^{-3}$ , and as the peak doping concentration decreased, the  $\rho_c$  increased rapidly.<sup>21</sup> In this case, contact on the lowly doped emitter “through Ag crystallites” will result in much higher  $\rho_c$ . Thus, the lowly doped emitter exhibits high  $\rho_c$ , and hence, “through Ag crystallites,” carrier transport is not suitable for the carrier transport mechanism.

The other carrier transport path is “through an ultrathin IGL”<sup>23</sup> of 1–3.6 nm and a thicker IGL of 5–20 nm with discontinuous Ag nanoparticles.<sup>21</sup> However, to realize uniform IGL throughout the entire metal contact is challenging, and the alternative would be for the IGL to be conductive. Hence, in order to achieve ohmic contact on a lowly doped emitter, it is imperative that the IGL must be conductive. In addition, this would be a preferred transport path, which is independent of the peak carrier concentration. Thus, it is important to further develop understanding of the appropriate carrier transport path at the Ag/Si interface for screen-printed Ag pastes. This work, therefore, focuses on developing an understanding of the carrier transport path for a lowly doped emitter through microstructure [SEM with energy dispersive x-ray spectroscopy (EDS) and STEM] optical (Raman spectroscopy) and electrical [conductive atomic force microscopy (C-AFM)] analyses. More so, to validate the carrier transport path suggested by these analyses, a modified Fowler–Nordheim tunneling model was used to model the C-AFM I–V characteristic curves.

## II. EXPERIMENTAL METHODS

The boron-doped p-type 2.5  $\Omega\text{-cm}$  Cz single-crystalline Si wafers were first cleaned and then textured followed by  $\text{POCl}_3$  diffusion to form a 95  $\Omega/\text{sq}$  emitter with a near surface doping concentration of  $5 \times 10^{19} \text{ cm}^{-3}$ . After phosphorus glass removal, the ARC  $\text{SiN}_x$  layer (73 nm) was deposited by plasma-enhanced chemical vapor deposition (PECVD). Then, the back Al paste and the front Ag paste (commercial Ag paste containing  $\text{TeO}_2$  glass frits) were in turn screen printed and dried. After that, the Ag and Al contacts were co-fired in the rapid thermal processing (RTP) infrared belt furnace at 230 ipm under a 815  $^\circ\text{C}$  peak temperature.

Since the objective of this work was to investigate the Ag/Si gridline interface and to establish the carrier transport mechanism, the fabricated cells were cut into 3-mm strips and arranged in three sets: (i) with Ag gridline (Ag), (ii) the Ag metal removed by nitric acid ( $\text{HNO}_3$ ) to characterize IGL ( $\text{HNO}_3$ ), and (iii) the hydrofluoric acid (HF) dip to remove IGL (HF).

The microstructure, elemental composition, and the electrical property of the samples were evaluated by Field-Emission

SEM (FESEM) with EDS (FEI Verios 460L), STEM with EDS (FEI Talos F200X), and the Raman spectrometer (HORIBA, XploRa™PLUS) excited at 532 nm and C-AFM (Asylum MFP-3D).

## III. RESULTS AND DISCUSSION

### A. SEM/EDS and Raman spectrometer analyses

Figure 1(a) is a cross-sectional view of the Ag/Si interface showing the IGL thickness of  $>380 \text{ nm}$ . The bright part of the IGL indicates the embedded metal alloys. Figure 1(b) shows the side view of the interface glass layer embedded with micro-sized metal alloys. The inset in Fig. 1(b), top view, shows the glass layer underneath the metal gridline on the emitter after the Ag gridline is removed with  $\text{HNO}_3$ . Figure 1(c) is the EDS elemental analysis of the selected metal alloy in Fig. 1(b) (side view). It shows the constituent of the micro-sized alloys, which include Ag, Pb, and Te elements. Figure 1(d) shows the side view, and the inset shows the top view after HF dip, confirming the absence of the metal alloys. The Raman spectroscopy in Fig. 1(e) reveals the constituent of the micro-sized alloys as  $\text{Ag}_2\text{Te}$  and  $\text{PbTe}$  semimetal compounds according to the peaks<sup>24–26</sup> at 76  $\text{cm}^{-1}$ , 119  $\text{cm}^{-1}$ , 145  $\text{cm}^{-1}$ , and 183  $\text{cm}^{-1}$ . Other peaks in Fig. 1(e) at around 390  $\text{cm}^{-1}$  and 660  $\text{cm}^{-1}$  belong to  $\text{TeO}_2$  glass.<sup>26</sup>

The redox reactions that resulted in the formation of the micro-sized alloys ( $\text{Ag}_2\text{Te}$  and  $\text{PbTe}$ ) are given below in reactions (1)–(6). The calculated thermodynamic potential for these reactions was reported in our earlier work.<sup>27</sup>

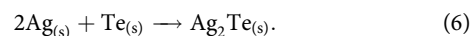
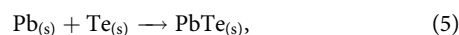
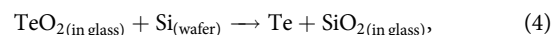
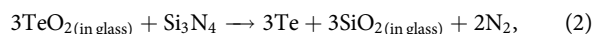
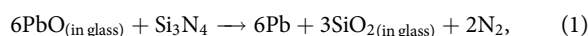
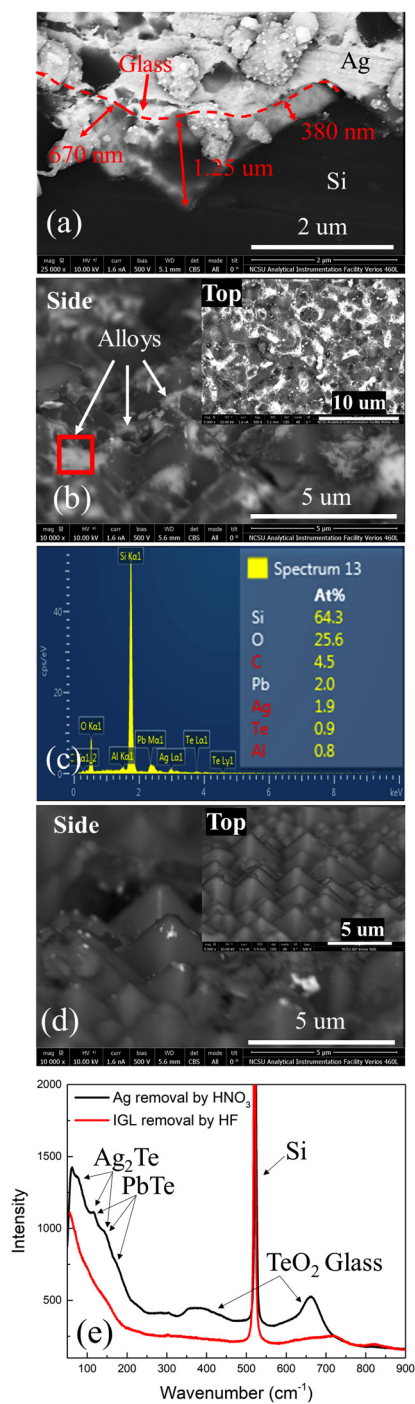


Figure 1(d) shows the SEM side and top views of the sample that was dipped in HF to remove the interface glass layer, which contained the metal alloys. Clean Si pyramids are revealed without the alloys as in Fig. 1(b) before the interface glass layer was removed in HF.<sup>27–29</sup> Furthermore, large Ag crystallites<sup>1,12</sup> were not observed. Thus, the clean Si pyramids indicate that semimetal compounds are embedded in the glass layer and not in Si. This confirms the Raman spectroscopy micrographs after HF treatment, which did not show the  $\text{Ag}_2\text{Te}$ ,  $\text{PbTe}$ , and  $\text{TeO}_2$  peaks. Therefore, the  $\text{Ag}_2\text{Te}$  and  $\text{PbTe}$  alloys are encapsulated in the thick IGL and behave as a bridge for carrier transport from the Si to Ag gridline. This is akin to the metal precipitates formed after forming gas anneal to reduce contact resistance,<sup>18</sup> but forming gas anneal reduces the gridline contact adhesion. However, these alloys in the IGL do not affect the gridline adhesion. Note that the semimetals are formed



**FIG. 1.** SEM images of (a) a cross-sectional view of the Ag/Si interface with Ag gridlines, (b) the side view and the top view (up right) of the interface after HNO<sub>3</sub> treatment, (c) the EDS analysis of the selected area [marked in red box in (b)], and (d) the side view and the top view (up right) of the interface after HF treatment, and (e) the Raman spectroscopy of the sample after HNO<sub>3</sub> and HF treatment.

spontaneously according to the chemical reaction equations [Eqs. (1)–(6)]<sup>27</sup> without an extra annealing process.

### B. STEM/EDS analyses

The distribution of the semimetal nanoparticles in the IGL was assessed with STEM micrographs after the Ag gridlines were removed in HNO<sub>3</sub>. Figure 2(a) shows the IGL with a thickness of ~1.3 μm, which agrees with the SEM micrograph analysis of Fig. 1(a). An IGL thickness of this magnitude will impede the carrier transport to the Ag gridlines. Also, the thickness of the semimetal nanoparticles embedded in the IGL was measured as

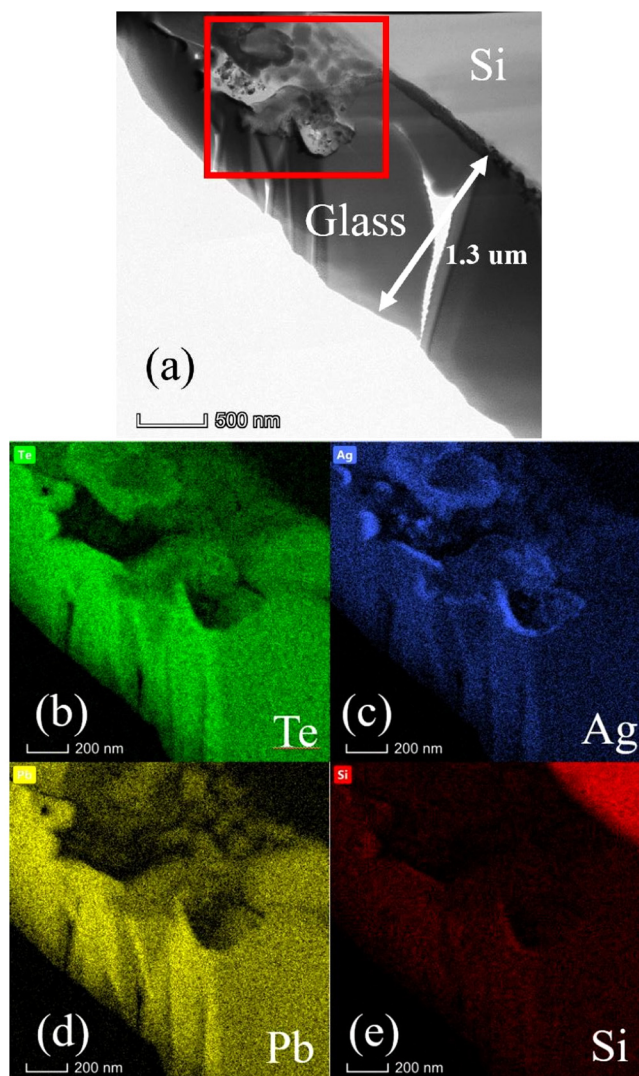


**FIG. 2.** (a) STEM image of the glass cross section and the elemental analysis of the selected area (marked in a red box) based on (b) Te (green), (c) Ag (blue), (d) Pb (yellow), and (e) Si (red).

$\sim 0.9$   $\mu\text{m}$ . According to Figs. 2(b)–2(e), Ag, Pb, and Te are the three dominant elements found in the IGL. These three elements are mixed with each other according to the features' shapes under different colors in the figures. However, each element was not evenly distributed in the IGL because of the same map, and some areas are brighter than others, especially in Fig. 2(c). Figures 2(b)–2(d) show no diffusion of elements (Ag, Pb, and Te) into the Si emitter compared to Fig. 2(e) where the Si emitter contains more Si elements than in the IGL. Due to the presence of these three elements in the glass and based on the peaks shown in the Raman spectroscopy, the semimetals were formed in the IGL, and the features in the red box in Fig. 2(a) can be concluded to be semimetal compounds of  $\text{Ag}_2\text{Te}$  and  $\text{PbTe}$ . Thus, these semimetal nanoparticles contact the Si emitter and the Ag gridlines and form a conductive bridge to provide a carrier conduction pathway.

### C. Conductive-AFM analyses

The conductivity of the IGL was mapped by conductive-AFM as shown in Fig. 3(a). The white micro-sized feature represents the highly conductive area on the IGL with current larger than 10 nA under a  $\pm 10$  V bias. This conductive feature was located on top of the Si pyramid according to Fig. 3(c). Based on the shape, size, and location, this conductive area matches the alloys found in Fig. 1(b) (top view). The I–V characteristic curves measured by C-AFM [Fig. 3(d)] established an ohmic contact on the alloyed region, while the rest of the glass area was non-conductive. The specific contact resistance of the alloy was calculated based on the slope of the C-AFM I–V curves and the contact area.<sup>29</sup> The value ranged from  $4.93 \times 10^{-4}$  to  $26.94 \times 10^{-4} \Omega \text{cm}^2$ , which is comparable to that of Ag crystallites<sup>14</sup> ( $2 \times 10^{-4} \Omega \text{cm}^2$ ). Here, due to the dielectric property of the glass itself and the non-uniform distribution of the semimetals in the glass, the overall specific contact resistance of the semimetals is somewhat higher than that of Ag crystallites. However, the formed semimetal nanoparticles in the IGL dramatically increased its conductivity and form a conductive path to transport carriers from Si to the Ag gridline. In addition, these semimetals do not have the tendency or risk of penetrating the p-n junction as Ag crystallites would, if they are very large. The carrier transport pathway, “through the conductive bridge,” was found to be suitable for lowly doped emitters.

### D. Mathematical model of semimetal nanoparticle assisted contact

Based on the microstructure observed by SEM and STEM micrographs of Figs. 1(b) (side view) and 2(a), respectively, the schematic view of the semimetal nanoparticles assisted contact is shown in Fig. 4(a). Instead of carriers tunneling through the IGL, the carriers are conducted through the bridge formed by the embedded semimetal nanoparticles in the IGL.

In order to confirm the carrier transport path by the semimetal nanoparticle assisted contact, C-AFM I–V characteristics were modeled according to the modified Fowler–Nordheim tunneling

(FNT)<sup>30–32</sup> given as

$$I(V) = \frac{A_{\text{eff}} q^3 V^2 m}{8\pi h \Phi_B d^2 m_0} \cdot \exp\left(\frac{-8\pi\sqrt{2m_0}\Phi_B^{1.5}d}{3hV} \cdot v(V)\right), \quad (7)$$

where

$$v(V) = \frac{0.96V}{\Phi_B}. \quad (8)$$

$v(V)$  in Eq. (7) is the correction factor when  $V > \Phi_B/q$ ,  $A_{\text{eff}}$  is the effective contact area,  $q$  is the electron charge,  $V$  is the applied voltage,  $m$  is the free electron mass,  $h$  is Planck's constant,  $\Phi_B$  is the barrier height,  $d$  is the glass thickness, and  $m_0$  is the effective electron mass.

According to Ref. 21,

$$\rho_c = \left(\frac{\partial J}{\partial V}\right)_{V=0}^{-1}. \quad (9)$$

Thus,

$$\rho_c = \left(\frac{q^3 V m}{4\pi h \Phi_B d^2 m_0} \cdot \exp\left(\frac{-2.56\pi d \sqrt{2m_0}\Phi_B}{h}\right)\right)^{-1}. \quad (10)$$

Figure 4(b) shows that the modeled (dashed) and measured I–V (solid) curves are in good agreement. A glass thickness of 17.2–21.5 nm fits the measured I–V curves, and the thickness is in the upper limit of the glass thickness (20 nm)<sup>21</sup> for the tunneling carrier transport mechanism. However, it is less than one tenth the measured glass thickness ( $>380$  nm) shown by the SEM micrograph in Fig. 1(a). Thus, by fitting the curve with only  $\sim 18$  nm glass thickness, it confirms that the semimetal nanoparticles increased the conductivity of the thick IGL, which in turn provided a bridge that the carriers transport through. Moreover, the higher transport current around the center of the conductive area than around the edge suggests that the center of the conductive area had a higher density of semimetal nanoparticles.

Also, in Fig. 4(b), the calculated barrier height for the contact is 0.1 eV. The low barrier height can be attributed to the presence of the  $\text{PbTe}$  and  $\text{Ag}_2\text{Te}$  semimetal nanoparticles. The bandgap of  $\text{PbTe}$  is  $\sim 0.30$  eV,<sup>33,34</sup> while that of  $\text{Ag}_2\text{Te}$  is  $\sim 0.014$  eV at 300 K.<sup>35,36</sup> Both  $\text{PbTe}$  and  $\text{Ag}_2\text{Te}$  are n-type<sup>37,38</sup> because of the excess Pb in  $\text{PbTe}$  and excess Ag in  $\text{Ag}_2\text{Te}$ . The work function of  $\text{PbTe}$  is  $\sim 4.30$  eV,<sup>39</sup> however, the work function of  $\text{Ag}_2\text{Te}$  has not been fully studied. Based on the photoemission spectrum of  $\text{Ag}_2\text{Te}$ <sup>40</sup> and the energy band diagram of the Si/ $\text{PbTe}$  contact<sup>41</sup> and the  $\text{PbTe}/\text{Ag}_2\text{Te}$  contact,<sup>42</sup> the energy band diagram of the Ag/semimetal nanoparticles (in IGL)/Si contact can be modeled as shown in Fig. 5. The energy band diagram shows the conduction band alignment between semimetal nanoparticles and Si and a low barrier height between Ag and semimetal nanoparticles. Here, the overall low barrier height (0.1 eV) results from the semimetal nanoparticle “bridge” at the Ag/Si interface. Compared with the measured barrier height ( $\sim 0.65$  eV)<sup>43</sup> of Ag/n-Si (100  $\Omega/\text{sq}$ ), the barrier height through the semimetal nanoparticle “bridge” (0.1 eV) is low enough

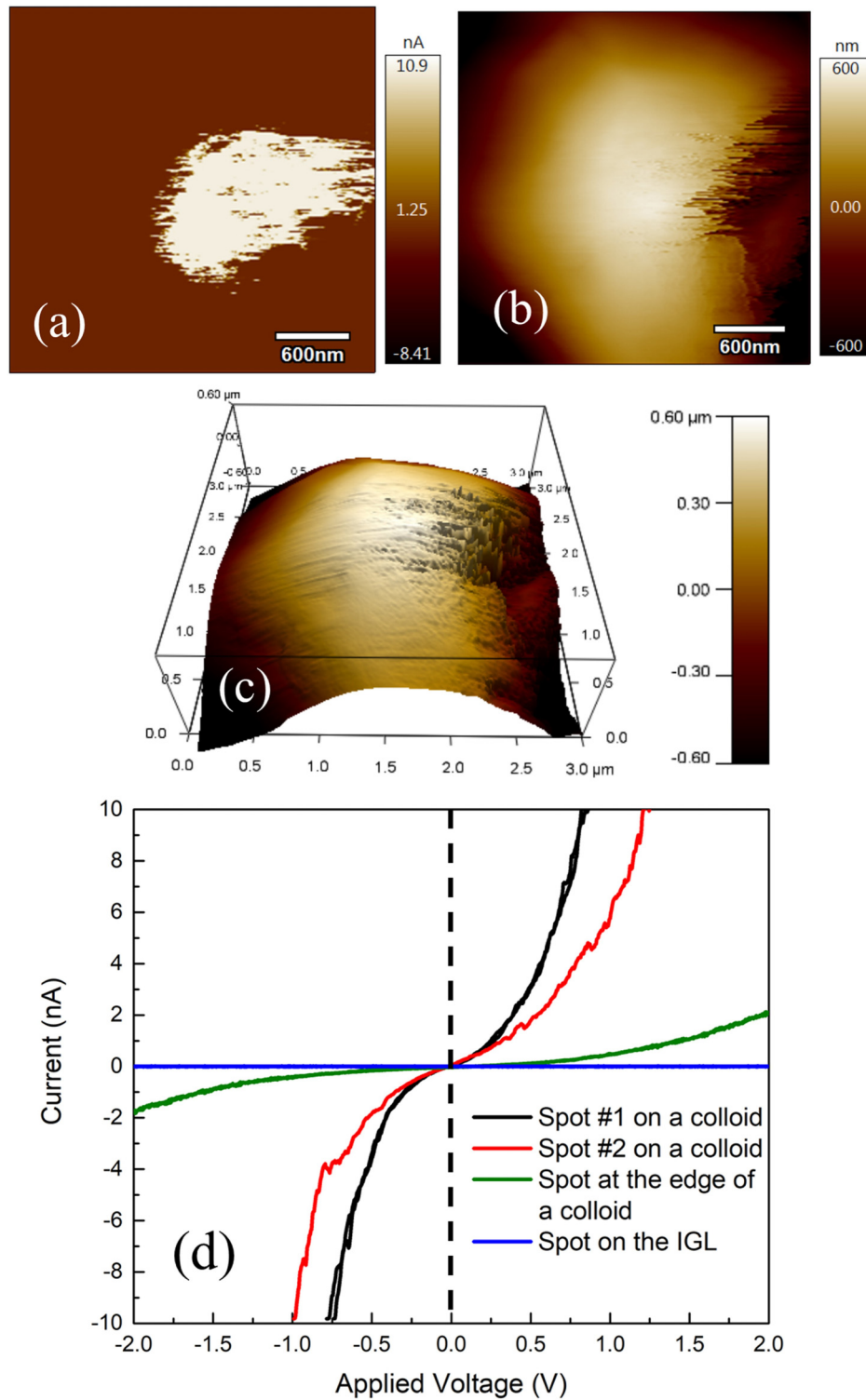


**FIG. 3.** Conductive-AFM images of the sample after  $\text{HNO}_3$  treatment based on the (a) current, (b) height, (c) 3D, and (d) I-V curves of the conductive areas and the nearby nonconductive area.

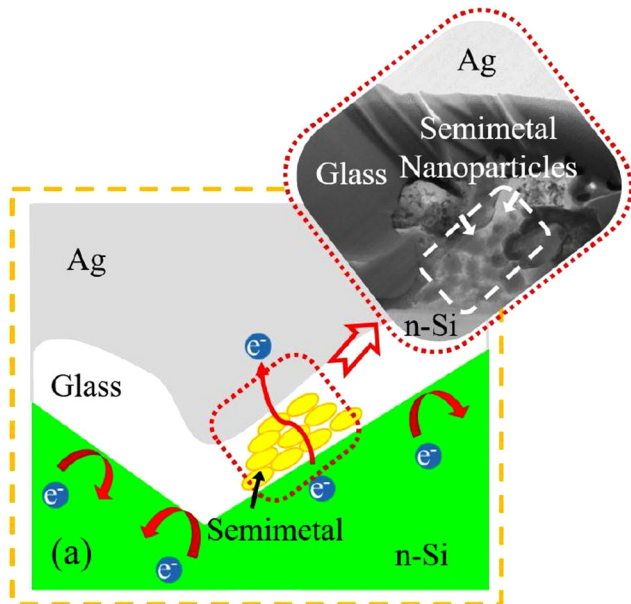


FIG. 4. (a) Schematic of the Si pyramids with semimetal nanoparticles in the thick IGL [the STEM image is from Fig. 2(a)]. (b) Measured and calculated I-V curves for the top and edge of the colloid. The modeled barrier height and the glass thickness are indicated.

to exclude the impact of the Si doping concentration. Although the actual contact between semimetal nanoparticles can be more complicated, as the barrier height is not a function of the Si doping concentration, the specific contact resistance can be calculated based on Eq. (10) and is independent of the Si doping concentration.

Figure 6 is generated from Eq. (7), and it shows the impact of the barrier height and IGL thickness on the current transport. Although an IGL of ~18 nm thickness and a barrier height of  $\Phi_B = 0.1$  eV fit the C-AFM I-V curves in Figs. 6(a) and 6(b), a slight increase in the barrier height and the IGL thickness can significantly decrease the current transport. Thus, the presence of  $\text{Ag}_2\text{Te}$  and  $\text{PbTe}$  semimetal nanoparticles in the IGL at a high density is crucial for higher current transport.

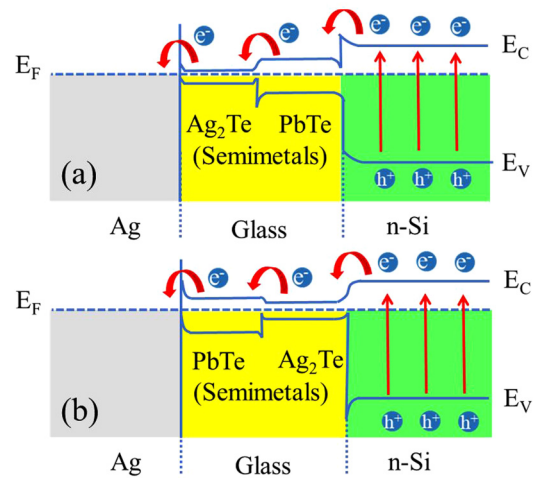


FIG. 5. Energy band diagram of Ag/semimetal nanoparticles (in IGL)/Si contact: (a) Ag/ $\text{Ag}_2\text{Te}$ / $\text{PbTe}$ /Si contact and (b) Ag/ $\text{PbTe}$ / $\text{Ag}_2\text{Te}$ /Si contact.

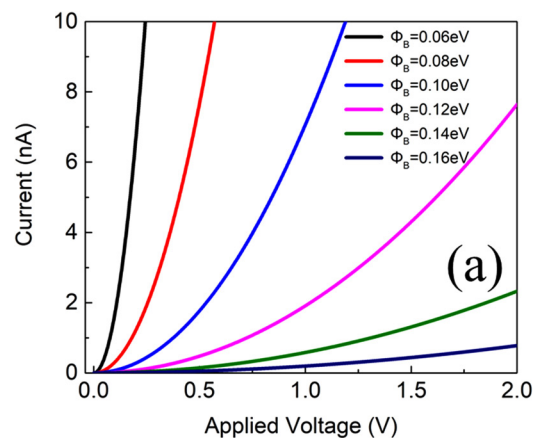
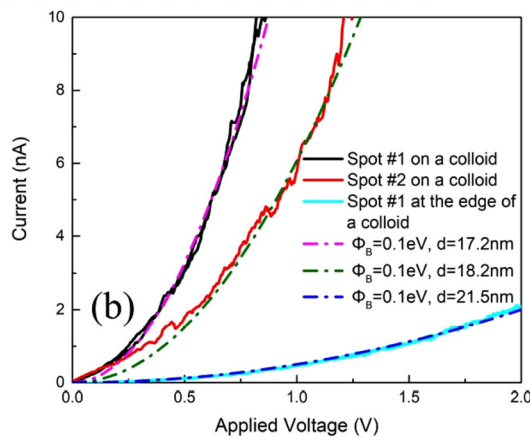


FIG. 6. Calculated I-V curves of resonant tunneling based on the (a) barrier height and (b) glass thickness.

## IV. CONCLUSION

In this work, ohmic contact formed by embedded semimetal nanoparticles in the thick IGL at the Ag/Si contact interface was studied. It was established that the embedded alloys enhanced the conductivity of the IGL, and this constituted a new carrier transport path for a lightly doped emitter, which is independent of the peak surface carrier concentration. According to the SEM and STEM, an IGL with a thickness of  $\geq 380$  nm was measured and found to contain a large amount of micro-sized alloys, which were composed of semimetal nanoparticles. These semimetal nanoparticles were identified as Ag<sub>2</sub>Te and PbTe, which possess low bandgaps. The presence of these low bandgap compounds in accordance with the C-AFM measured I-V characteristic curves led to the high transport current from Si to gridlines. By modeling a modified Fowler-Nordheim tunneling process in conjunction with the measured C-AFM I-V characteristic curves, a barrier height of 0.1 eV and an IGL thickness of  $\sim 18$  nm were obtained. This is contradictory to the measured IGL thickness, which would result in a very high contact resistance under a barrier height of 0.65 eV. However, the modeled glass thickness suggests that the presence of semimetal nanoparticles with a low bandgap lowered effectively the overall contact barrier height and increased the IGL conductivity so that the IGL thickness is inconsequential. These semimetal nanoparticles acted as a bridge to transport carriers from Si to Ag. This new carrier transport path is independent of the IGL thickness and the emitter doping concentration, which is critical to achieve ohmic contact on the lowly doped emitter for next-generation Si solar cells.

## DATA AVAILABILITY

The data that support the findings of this study are available from the corresponding author upon reasonable request.

## REFERENCES

- G. Schubert, F. Huster, and P. Fath, "Current transport mechanism in printed Ag thick film contacts to an N-type emitter of a crystalline silicon solar cell," in *EU PVSEC Proceedings* (WIP GmbH & Co Planungs-KG, 2004), pp. 813–816.
- R. Hoenig, M. Duerrschnebel, W. van Mierlo, Z. Aabdin, J. Bernhard, J. Biskupek, O. Eibl, U. Kaiser, J. Wilde, F. Clement *et al.*, *Energy Procedia* **43**, 27–36 (2013).
- Z. Li, L. Liang, and L. Cheng, *J. Appl. Phys.* **105**, 066102 (2009).
- E. Cabrera, S. Olibet, J. Glatz-Reichenbach, R. Kopecek, D. Reinke, and G. Schubert, *J. Appl. Phys.* **110**, 114511 (2011).
- M. M. Hilali, K. Nakayashiki, C. Khadilkar, R. C. Reedy, A. Rohatgi, A. Shaikh, S. Kim, and S. Sridharan, *J. Electrochem. Soc.* **153**, A5–A11 (2006).
- D. Kim, S. Hwang, and H. Kim, *J. Korean Phys. Soc.* **55**, 1046–1050 (2009).
- S. Watanabe, T. Kodaera, and T. Ogihara, *J. Cera. Soc. Jpn.* **124**, 218–222 (2016).
- P. Kumar, M. Pfeiffer, B. Willsch, O. Eibl, L. J. Koduvelikulathu, V. D. Mihailetchi, and R. Kopecek, *Sol. Energy Mater. Sol. Cells* **157**, 200–208 (2016).
- W.-H. Lee, T.-K. Lee, and C.-Y. Lo, *J. Alloys Compd.* **686**, 339–346 (2016).
- C. Ballif, D. Huljic, G. Willeke, and A. Hessler-Wyser, *Appl. Phys. Lett.* **82**, 1878–1880 (2003).
- S.-B. Cho, K.-K. Hong, J.-Y. Huh, H. J. Park, and J.-W. Jeong, *Curr. Appl. Phys.* **10**, S222–S225 (2010).
- S. Kontermann, G. Emanuel, J. Benick, R. Preu, and G. Willeke, "Characterisation of silver thick-film contact formation on textured monocrystalline silicon solar cells," in *EU PVSEC Proceedings* (WIP GmbH & Co Planungs-KG, 2006), pp. 613–616.
- G. Grupp, D. Huljic, R. Preu, G. Willeke, and J. Luther, "Peak firing temperature dependence of the microstructure of Ag thick-film contacts on silicon solar cells—a detailed AFM study of the interface," in *EU PVSEC Proceedings* (WIP GmbH & Co Planungs-KG, 2005), pp. 1379–1382.
- S. Kontermann, G. Willeke, and J. Bauer, *Appl. Phys. Lett.* **97**, 191910 (2010).
- S. Kontermann, R. Preu, and G. Willeke, *Appl. Phys. Lett.* **99**, 111905 (2011).
- C.-H. Lin, S.-Y. Tsai, S.-P. Hsu, and M.-H. Hsieh, *Sol. Energy Mater. Sol. Cells* **92**, 1011–1015 (2008).
- Z. Li, L. Liang, A. Ionkin, B. Fish, M. Lewittes, L. Cheng, and K. Mikeska, *J. Appl. Phys.* **110**, 074304 (2011).
- G. Schubert, J. Horzel, and S. Ohl, "Investigations on the mechanism behind the beneficial effect of a forming gas anneal on solar cells with silver thick film contacts," in *EU PVSEC Proceedings* (WIP GmbH & Co Planungs-KG, 2006), p. 1460.
- J. Trube, *International Technology Roadmap for Photovoltaic (ITRPV)*, 9th ed. (VDMA PV Equipment, 2018).
- A. M. Svensson, S. Olibet, D. Rudolph, E. Cabrera, J. Friis, K. Butler, and J. Harding, *J. Electrochem. Soc.* **161**, E3180–E3187 (2014).
- H. Yang, H. Wang, X. Lei, C. Chen, and D. Cao, *Int. J. Numer. Model.* **27**, 649–655 (2014).
- A. Yu, *Solid-State Electron.* **13**, 239–247 (1970).
- H. Nakatsujii, A. Shimizu, and Y. Omura, *Superlattices Microstruct.* **28**, 425–428 (2000).
- A. Qin, Y. Fang, P. Tao, J. Zhang, and C. Su, *Inorg. Chem.* **46**, 7403–7409 (2007).
- T. Milenov, T. Tenev, I. Miloushev, G. Avdeev, C. Luo, and W. Chou, *Opt. Quantum Electron.* **46**, 573–580 (2014).
- B. Zhang, C. Cai, H. Zhu, F. Wu, Z. Ye, Y. Chen, R. Li, W. Kong, and H. Wu, *Appl. Phys. Lett.* **104**, 161601 (2014).
- K. Ren, T. Ye, Y. Zhang, and A. Ebong, *MRS Adv.* **4**, 311–318 (2019).
- K. Ren, D. Han, Y. Tang, Y. Zhang, and A. Ebong, in *IEEE PVSC* (IEEE, 2019), pp. 3243–3247.
- K. Ren, D. Han, and A. Ebong, "Electrical characterization of nano-colloids in Si solar cell screen-printed contacts by conductive atomic force microscopy (C-AFM)," in *EU PVSEC Proceedings* (WIP GmbH & Co Planungs-KG, 2019), pp. 286–289. <https://www.eupvsec-proceedings.com/proceedings/fulltext=Fire&paper=48575>.
- D. Xu, G. D. Watt, J. N. Harb, and R. C. Davis, *Nano Lett.* **5**, 571–577 (2005).
- W. Frammelsberger, G. Benstetter, J. Kiely, and R. Stamp, *Appl. Surf. Sci.* **252**, 2375–2388 (2006).
- W. Frammelsberger, G. Benstetter, J. Kiely, and R. Stamp, *Appl. Surf. Sci.* **253**, 3615–3626 (2007).
- K. Ahn, C. Li, C. Uher, and M. G. Kanatzidis, *Chem. Mater.* **21**, 1361–1367 (2009).
- P. Rawat, B. Paul, and P. Banerji, *Materials and Processes for Energy: Communicating Current Research and Technological Developments* (Formatex Research Center, 2013).
- F. Aliev, E. Kerimova, and S. Aliev, *Semiconductors* **36**, 869–873 (2002).
- M. Jafarov, F. Aliev, R. Hasanova, and A. Saddinova, *Semiconductors* **46**, 861–865 (2012).
- M. Bala, S. Gupta, T. Tripathi, D. Avasthi, and K. Asokan, *AIP Conf. Proc.* **1665**, 110047 (2015).
- S. A. Aliev and F. F. Aliev, *Izvestiya Akademii Nauk SSSR, Neorganicheskoe Materialy* **25**, 241–246 (1989). [https://inis.iaea.org/search/search.aspx?orig\\_q=RN:21009816](https://inis.iaea.org/search/search.aspx?orig_q=RN:21009816).
- T. Li and W. A. Schroeder, "PbTe(111) sub-thermionic photocathode: A route to high-quality electron pulses," *arXiv:1704.00194* (2017).
- S. Kashida, N. Watanabe, T. Hasegawa, H. Iida, and M. Mori, *Solid State Ion.* **148**, 193–201 (2002).
- I. C. Urbiola, R. R. Bon, and Y. Vorobiev, *IEEE Sens. J.* **16**, 5875–5882 (2016).
- H. Yang, J.-H. Bahk, T. Day, A. M. Mohammed, G. J. Snyder, A. Shakouri, and Y. Wu, *Nano Lett.* **15**, 1349–1355 (2015).
- R. Balsano, A. Matsubayashi, and V. P. LaBella, *AIP Adv.* **3**, 112110 (2013).